# Wafer-Scale Growth of Single-Crystal Monolayer Graphene on Reusable Hydrogen-Terminated Germanium

Jae-Hyun Lee,[1,2,3]* Eun Kyung Lee,[4]* Won-Jae Joo,[3,4]* Yamujin Jang,[2,3] Byung-Sung Kim,[1,3] Jae Young Lim,[1,3] Soon-Hyung Choi,[2,3] Sung Joon Ahn,[5] Joung Real Ahn,[1,5] Min-Ho Park,[2] Cheol-Woong Yang,[2] Byoung Lyong Choi,[4]† Sung-Woo Hwang,[3,4]† Dongmok Whang[1,2,3]†

The uniform growth of single-crystal graphene over wafer-scale areas remains a challenge in the commercial-level manufacturability of various electronic, photonic, mechanical, and other devices based on graphene. Here, we describe wafer-scale growth of wrinkle-free single-crystal monolayer graphene on silicon wafer using a hydrogen-terminated germanium buffer layer. The anisotropic twofold symmetry of the germanium (110) surface allowed unidirectional alignment of multiple seeds, which were merged to uniform single-crystal graphene with predefined orientation. Furthermore, the weak interaction between graphene and underlying hydrogen-terminated germanium surface enabled the facile etch-free dry transfer of graphene and the recycling of the germanium substrate for continual graphene growth.

The availability of high-quality, large, single-crystal Si wafers is fundamental to current Si-based electronics. Given that the potential advantages of graphene as a host material for various devices have been established, the primary requirement is cost-efficient, reliable, and high-throughput synthesis of single-crystal monolayer graphene over wafer-scale dimensions with methods compatible with current semiconductor technology. In addition, single-crystal graphene with a predefined orientation will allow various applications of graphene's orientation-dependent properties (1, 2). Various methods for synthesizing large-area graphene monolayers have been reported, including the graphitization of silicon carbide surfaces (3, 4) and catalytic chemical vapor deposition (CVD) on metals (5–7). In particular, CVD has been used to synthesize predominantly large-area monolayer graphene of excellent quality on polycrystalline copper foils (5) that can easily be transferred to other substrates. However, the large-scale synthetic graphene produced thus far are typically polycrystalline, consisting of many single-crystalline grains separated by defective grain boundaries that degrade their electrical and mechanical properties (8, 9).

There are two possible approaches to catalytic growth of a single-crystal graphene layer over a solid substrate surface. The first approach involves growing a single grain to as large a size as possible from a single nucleation site. The growth of a centimeter-size single-crystal graphene domain from a single nucleus was recently demonstrated (10). However, this approach may not be practical for reproducible and high-throughput synthesis of wafer-scale single-crystal graphene. The second approach involves the catalytic and epitaxial growth of graphene on a single-crystal substrate. If initial multiple nucleation of the graphene seeds occurs but with perfect rotational alignment, the unidirectionally aligned seeds can grow and coalesce into a uniform single-crystal layer without grain boundary defects, even if the nucleation density is high (Fig. 1A and fig. S1) (11). The epitaxial graphene growth has been extensively investigated with various single-crystal substrates (7, 12–14). However, wafer-scale single-crystal monolayer graphene has not yet been realized. Recent studies on the nucleation of graphene on a weakly interacting metal surface have demonstrated that the interaction between the metal surface and the graphene edge is responsible for the orientation determination of graphene seeds at the early stage of graphene growth (15). These results indicate that uniaxial and reversible binding of the seed edge on the catalytic surface is critical for the growth of single-crystal graphene from multiple nucleations.

If possible, a Si single-crystal wafer is an ideal substrate for the epitaxial graphene growth, because it is readily available up to 450 mm in diameter. However, the low carbon diffusivity on Si surface and the relatively high carbon solubility hamper the direct growth of high-quality monolayer graphene on Si (16). Instead of Si, we used a single-crystal Ge surface for the growth of single-crystal graphene, because of (i) its catalytic activity, which can lower the energy barriers for the catalytic decomposition of carbon precursor and thus can induce formation of graphitic carbon on the surface (17); (ii) the extremely low solubility of carbon in Ge even at its melting temperature ($<10^8$ atoms/cm$^3$) (18), enabling growth of complete monolayer graphene (19); (iii) the

well-defined and anisotropic atomic arrangement of single-crystal Ge surface, enabling aligned growth of multiple seeds that can merge into single-crystal layer without producing grain boundaries; (iv) the availability of a large-area single-crystal surface via epitaxial Ge growth on Si wafers (20); and (v) the small difference in thermal expansion coefficients between Ge and graphene, suppressing intrinsic wrinkle formation (21, 22).

For single-crystal graphene growth from the aligned seeds, we selected a Ge(110) substrate having anisotropic twofold in-plane surface symmetry. The graphene islands at the early stage of growth on H-terminated Ge(110) surface were uniaxially aligned along the [$\bar{1}$10] direction of the underlying Ge(110) surface (Fig. 1B) and then grown to form uniform monolayer graphene on an entire growth substrate (Fig. 1C and fig. S2). The single-crystal Ge layers were epitaxially grown on a Si(110) wafer (fig. S3), then highly uniform monolayer graphene was synthesized on the hydrogen-terminated Ge surfaces via a controlled low-pressure CVD by flowing a $CH_4$ gas (1 to 2% diluted in $H_2$) at 900° to 930°C (11). The chemisorption of H and C atoms on the Ge surface can be reversible at high temperature, enabling the catalytic growth of graphene on the H-terminated Ge surface (fig. S4). The highly symmetric C 1s core peak at a binding energy of 284.4 eV and the absence of Ge-C related peaks in the XPS spectra of the as-grown graphene on Ge surface imply that the carbon atoms in the graphene are fully sp$^2$-hybridized without a bonding interaction with the underlying Ge surface (fig. S5).

A high-resolution transmission electron microscopy (HR-TEM) image of the graphene reveals that well-defined monolayer graphene was formed without any noticeable structural defects (Fig. 1D). The overlaid selected area electron diffraction (SAED) patterns acquired from four different points separated from each other by ~2 μm illustrate that all of the points had the same crystallographic orientations, displaying a single-crystalline lattice structure of the graphene (Fig. 1D, inset). The cross-sectional TEM image in Fig. 1E also indicates that the as-grown graphene is monolayered. The low-energy electron diffraction (LEED) pattern of graphene grown on Ge(110) revealed six hexagonally arranged spots that correspond to single-crystal graphene (Fig. 2A). The positions of the LEED spots of graphene and the underlying Ge surface in Fig. 2A show that zigzag and armchair directions of graphene lattice are parallel to [001] and [$\bar{1}$10] directions of the Ge(110) facet, respectively (fig. S6). There were no satellite spots commonly observed for graphene epitaxially grown on a metal surface (12), suggesting the absence of interlayer bonding between graphene and the underlying Ge surface. We also investigated graphene growth on isotropic Ge(111) surface for comparative study. Growth on Ge(111) also produced monolayer graphene; however, the seed shapes are isotropic (fig. S7, A and B). Furthermore, the LEED

[1]SKKU Advanced Institute of Nanotechnology, Sungkyunkwan University (SKKU), Suwon 440-746, Korea. [2]School of Advanced Materials Science and Engineering, Sungkyunkwan University, Suwon 440-746, Korea. [3]Research Center for Time-Domain Nano-functional Devices, Samsung Advanced Institute of Technology, Yongin 449-712, Korea. [4]Nano Electronics Laboratory, Samsung Advanced Institute of Technology, Yongin 449-712, Korea. [5]Department of Physics, Sungkyunkwan University, Suwon 440-746, Korea.

*These authors contributed equally to this work.
†Corresponding author. E-mail: dwhang@skku.edu (D.W.); swnano.hwang@samsung.com (S.-W.H.); choibl@samsung.com (B.L.C.)

patterns (Fig. 2B) and TEM images (fig. S7) of graphene grown on Ge(111) indicate that the obtained graphene is polycrystalline with a weak domain orientation preference.

The Raman spectra of single-crystalline and polycrystalline graphene grown on Ge(110) and Ge(111) demonstrate that both materials are mono-layer graphene (23); however, the integrated in-tensity ratio between D and G peaks [$I$(D)/$I$(G)] of the single-crystal graphene (<0.03) is substantially smaller than that of the polycrystalline graphene (~0.4) (Fig. 2C), suggesting the absence of the ex-tended grain boundary defects in the single-crystal graphene on Ge(110) and its superior electrical properties. To evaluate the electrical characteristics of the single-crystalline and polycrystalline graphene, we fabricated back-gated graphene field-effect tran-sistors (GFETs) on $SiO_2$/Si substrates by using two different types of graphenes grown on Ge(110) and Ge(111) (fig. S8) (11). Compared with the GFET based on Ge(111)-catalyzed polycrystalline graphene, the single-crystal graphene exhibits smaller sheet resistances at the Dirac point with a narrower distribution (Fig. 2D). The carrier mo-bilities extracted from the sheet resistance by using the simple Drude model for single-crystal graphene were $7250 \pm 1390$ cm$^2$/V·s (SD) with a maximum value of 10,620 cm$^2$/V·s (Fig. 2E), which are comparable to the values of previ-ously reported metal-catalyzed single-domain graphene on Si/SiO$_2$ substrates (10, 24). The carrier mobility of the Ge-catalyzed polycrystal-line graphene ($2570 \pm 460$ cm$^2$/V·s) decreased because of grain boundary scattering. Consider-ing that typical nucleation density of Ge-catalyzed graphene (~10 per μm$^2$) is considerably higher than the densities reported for metal-catalyzed graphene (<0.1 per μm$^2$), the mobilities from the graphene grown on Ge(111) are still reasonably high, which suggests good intergrain connectivity in the polycrystalline graphene (8). Both prebake of the CVD chamber under H$_2$ flow and exces-sive H$_2$ flow during the growth were necessary to prepare the single-crystal graphene without a sub-stantial number of defects, indicating that even a trace amount of oxygen in the CVD chamber can affect the graphene growth results (fig. S9) (11).

These results demonstrate that the H-terminated Ge(110) surface is an ideal substrate for the cat-alytic growth of single-crystal graphene. The asym-metric twofold geometry of the Ge(110) surface and the anisotropic nature of the Ge-C covalent bonds dictate the perfect alignment of the edges
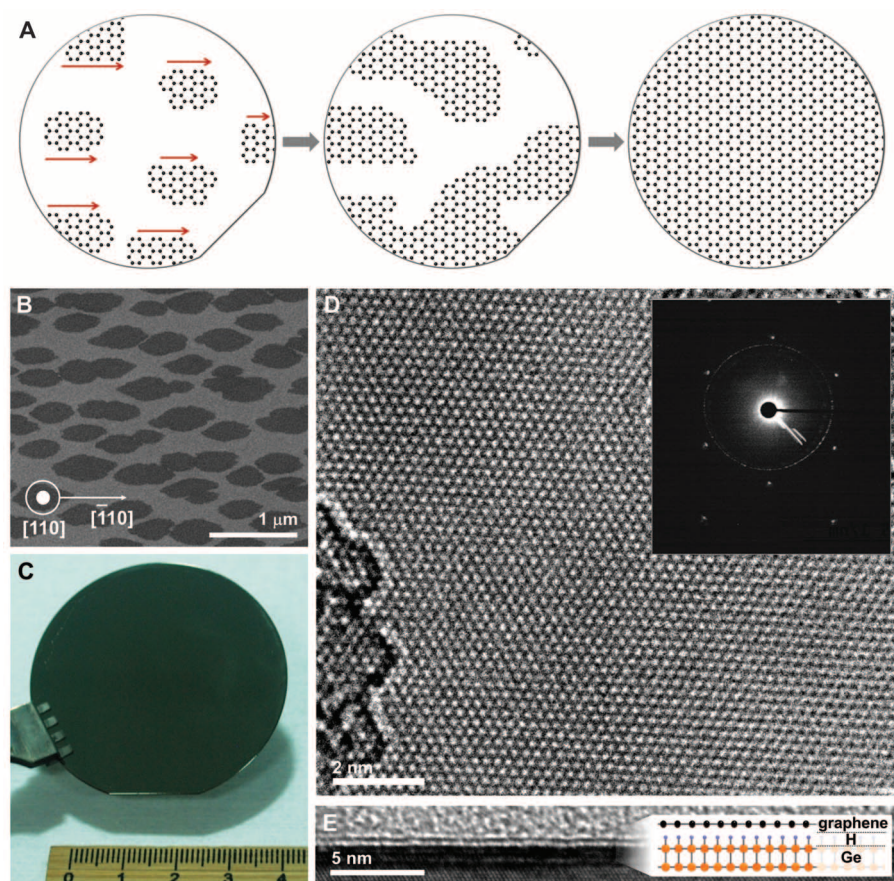


**Fig. 1. Single-crystal monolayer graphene grown on a hydrogen-terminated Ge(110) surface.** (**A**) A schematic illustration of catalytic growth of single-crystal monolayer graphene from unidirectionally aligned multiple seeds. (**B**) A typical SEM image of graphene seeds at the early stage of growth. (**C**) A photograph of graphene grown on a 5.08-cm Ge/Si (110) wafer. (**D**) A HR-TEM image of the single-crystal monolayer graphene. (Inset) Four overlaid SAED patterns, which were measured across the four different points. The distance between each point is ~2 μm. (**E**) A cross-sectional TEM image demonstrating that the as-grown graphene is monolayer. (Inset) A schematic illustration of the monolayer graphene grown on the H-terminated Ge surface.



**Fig. 2. Comparison of single-crystalline and polycrystalline graphene grown on H-terminated Ge(110) and Ge(111) surfaces.** (**A**) LEED pat-terns of single-crystal graphene grown on a H-Ge (110) substrate at 60 and 120 eV. The diameter of the electron beam was ~1 mm. (**B**) LEED patterns of polycrystalline graphene grown on a H-Ge(111) substrate at 60 and 120 eV. Gray circles in (A) and (B) denote the diffraction spots resulting from the Ge(110) and the Ge(111) substrate, respectively. (**C**) Raman spectra of single-crystal and polycrystal-line graphene grown on H-Ge(110) and H-Ge(111) surfaces under same growth conditions. a.u, arbi-trary units. (**D**) The distribution of sheet resistance ($R_{sh}$) at the Dirac point. The carrier mobility μ near the Dirac point ($n = 3 \times 10^{11}$ per cm$^2$).
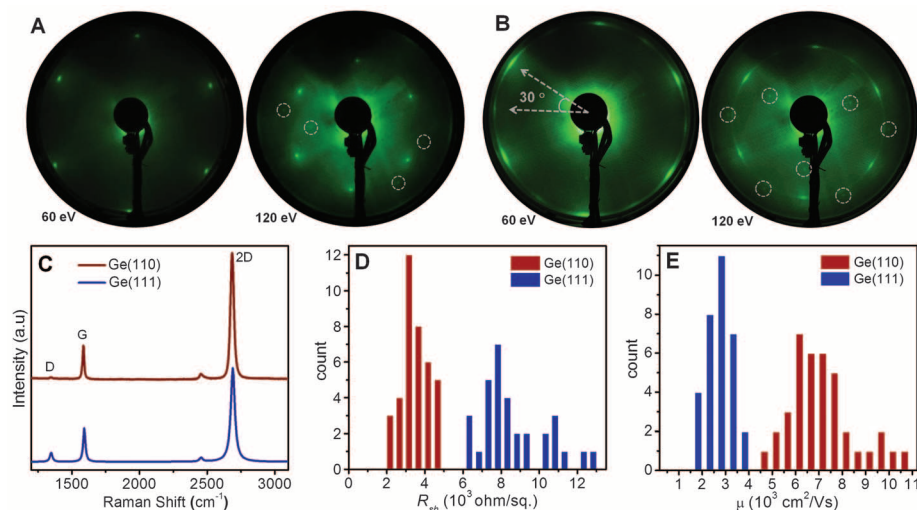
of graphene seeds at the early stage of growth (fig. S10), and such an orientation can be retained during further growth of the seeds to continuous single-crystal graphene layer because of the high barrier of graphene island rotation. When the edges of two adjacent graphene islands with same orientation approach each other before merging, atomic positions of the edges may not be well matched in our growth process. If the islands are tightly bound on the substrate surface, and thus the offset is not removed during coalesce of the islands, the positional displacement between the adjacent islands may form a nontilt grain boundary or extended line defect in spite of high formation energy of the extended defects in covalently bonded graphene (25). However, considering the pseudo–free-standing nature of the graphene islands on H-terminated Ge surface, the spontaneous formation of the extended grain-boundary defect during the growth of graphene on H-terminated Ge surface is highly unlikely. Figure 3 and fig. S2 show scanning electron microscopy (SEM) and TEM images of a typical edge front at which adjacent graphene islands are coalescing. In the reconstructed {1100} planes of the edge front (Fig. 3D), no discontinuous line was observed, indicating that adjacent islands are coalescing without grain boundary defects.

In addition to single crystallinity of graphene, wrinkle-free growth has been considered another challenge in graphene growth because the wrinkles cause scattering in the device characteristics and lead to inferior electrical properties (26). Wrinkles are known to be formed through thermal expansion mismatch because the underlying substrate contracts more than the graphene during postgrowth cooling, resulting in interlayer mechanical strain. However, as-grown graphene on a Ge substrate exhibited no wrinkles (fig. S11). We infer that the free-standing nature of graphene on the H-terminated surface and the relatively small difference in thermal expansion coefficient between the materials enabled the formation of flat graphene without wrinkles.

The extremely weak adhesion between graphene and the underlying substrate also allowed facile mechanical exfoliation of the graphene layer with few defects, regenerating the H-terminated Ge surface for further continual growth (figs. S12 and S13). Gold-coated graphene was easily exfoliated from the Ge surface, which shows that the binding energy between the graphene and the underlying Ge surface ($\gamma_{G\text{-}Ge}$) must be much less than 60 meV ($\gamma_{Au\text{-}G} \approx 60$ meV) (27). The merit of the mechanical exfoliation of monolayer graphene is apparent because catalytic single-crystal substrates are expensive to dispose and their chemical etchants are environmentally hazardous. Given research results that demonstrate the undesirable doping effect and physical damage on graphene caused by a wet transfer process, direct dry transfer without substrate etching appears even more favorable (28, 29). Figure 4A shows an optical image of the graphene that was mechanically exfoliated and transferred on the

SiO$_2$/Si substrate with 300-nm thermal oxide, indicating that the transferred graphene was a monolayer and wrinkle-free over the entire area. In addition, the Ge-catalyzed graphene exhibits transmittance of 97.64% at 550 nm (fig. S14), which agrees well with the ideal transmittance for monolayer graphene (30). Water contact angles of H-terminated Ge surface and Ge surface exposed after graphene delamination were almost identical (Fig. 4B and fig. S12), demonstrating the underlying Ge surface after graphene growth is hydrogen terminated. We repeated the growth

and etch-free dry transfer five times with the same H-terminated Ge/Si substrate, and the transferred graphene was evaluated by using Raman spectra (Fig. 4C). The Raman spectra of each of the graphene are almost identical, demonstrating that the single-crystal Ge substrate can be reused multiple times for graphene growth without degradation. Thus, the repeated, orientation-controlled synthesis of single-crystal monolayer graphene on the entire surface of a Si wafer using an H-terminated Ge buffer layer, in combination with complementary metal-oxide semiconductor–compatible etch-free
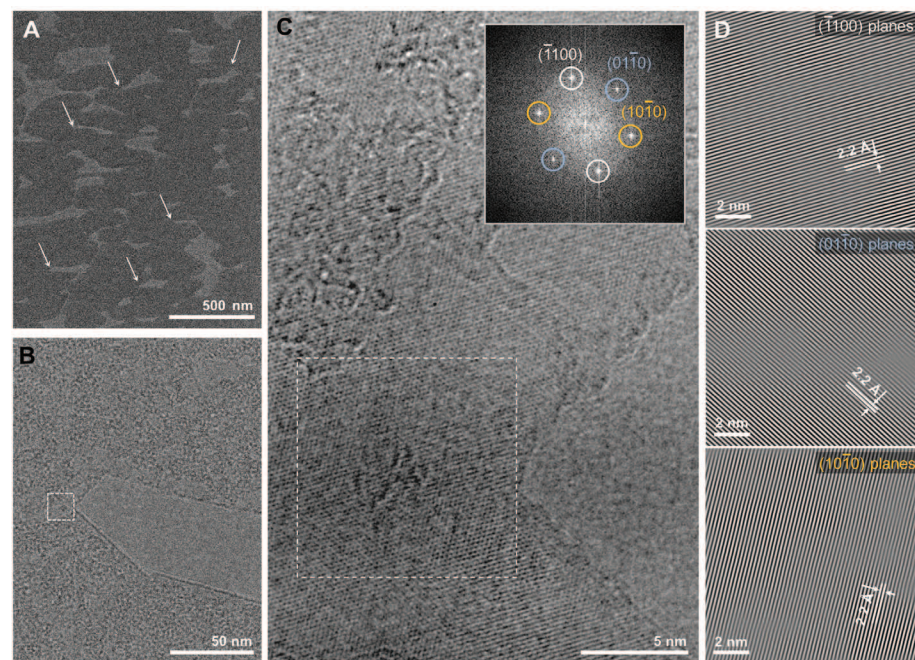


**Fig. 3. A graphene edge where adjacent graphene islands are merging.** (**A**) A SEM image of incompletely grown graphene on Ge(110). Arrows point out edge fronts at which adjacent islands are merging. (**B** and **C**) Bright-field TEM images of an edge front similar to the white arrows in (A). (C inset) A fast Fourier transform diffractogram taken from the region indicated by the dashed square in (B) and (C). (**D**) Three {1100} planes reconstructed from the three sets of diffraction spots in the (C) inset, showing no sign of grain boundary defects in the merged area.
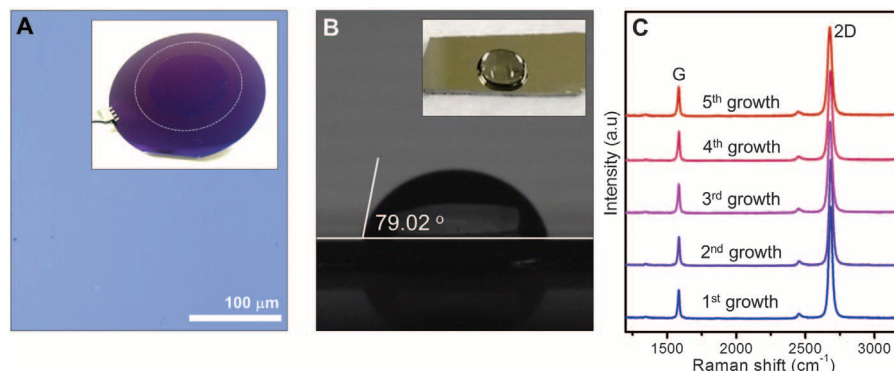


**Fig. 4. Etch-free dry transfer and repeated growth of single-crystal graphene on the same Ge/Si wafer.** (**A**) An optical image of graphene transferred onto a SiO$_2$/Si substrate with 300-nm thermal oxide. (Inset) A photograph of the 5.08-cm graphene transferred onto a 10.16-cm SiO$_2$/Si wafer. (**B**) Water droplet contact angle measurement on the H-terminated Ge surface exposed after mechanical peeling of the as-grown graphene. (Inset) A photograph of water droplet on the regenerated H-Ge surface. (**C**) Raman spectra of five different graphene layers grown by using the same Ge(110) substrates.

transfer processes, may open up commercial realization of various functional devices based on single-crystal graphene.

### References and Notes

1. A. K. Singh, B. I. Yakobson, *Nano Lett.* **9**, 1540–1543 (2009).
2. C. Zhang, L. Chen, Z. Ma, *Phys. Rev. B* **77**, 241402 (2008).
3. K. V. Emtsev et al., *Nat. Mater.* **8**, 203–207 (2009).
4. C. Berger et al., *Science* **312**, 1191–1196 (2006).
5. X. Li et al., *Science* **324**, 1312–1314 (2009).
6. K. S. Kim et al., *Nature* **457**, 706–710 (2009).
7. N. C. Bartelt, K. F. McCarty, *MRS Bull.* **37**, 1158–1165 (2012).
8. A. W. Tsen et al., *Science* **336**, 1143–1146 (2012).
9. Y. Wei et al., *Nat. Mater.* **11**, 759–763 (2012).
10. Y. Hao et al., *Science* **342**, 720–723 (2013).
11. Materials and methods are available as supplementary materials on *Science* Online.
12. P. W. Sutter, J.-I. Flege, E. A. Sutter, *Nat. Mater.* **7**, 406–411 (2008).
13. S. Nie, J. M. Wofford, N. C. Bartelt, O. D. Dubon, K. F. McCarty, *Phys. Rev. B* **84**, 155425 (2011).
14. Z. R. Robinson, P. Tyagi, T. R. Mowll, C. A. Ventrice Jr., J. B. Hannon, *Phys. Rev. B* **86**, 235413 (2012).
15. X. Zhang, Z. Xu, L. Hui, J. Xin, F. Ding, *J. Phys. Chem. Lett.* **3**, 2822–2827 (2012).
16. P. Thanh Trung et al., *Appl. Phys. Lett.* **102**, 013118 (2013).
17. P. W. Loscutoff, S. F. Bent, *Annu. Rev. Phys. Chem.* **57**, 467–495 (2006).
18. R. I. Scace, G. A. Slack, *J. Chem. Phys.* **30**, 1551–1555 (1959).
19. G. Wang et al., *Sci. Rep* **3**, 2465 (2013).
20. R. Lieten, S. Degroote, M. Leys, N. Posthuma, G. Borghs, *Appl. Phys. Lett.* **94**, 112113 (2009).
21. W. Bao et al., *Nat. Nanotechnol.* **4**, 562–566 (2009).
22. D. F. Gibbons, *Phys. Rev.* **112**, 136–140 (1958).
23. A. C. Ferrari, J. Robertson, *Phys. Rev. B* **61**, 14095–14107 (2000).
24. L. Gao et al., *Nat. Commun.* **3**, 699 (2012).
25. J. Lahiri, Y. Lin, P. Bozkurt, I. I. Oleynik, M. Batzill, *Nat. Nanotechnol.* **5**, 326–329 (2010).
26. W. Zhu et al., *Nano Lett.* **12**, 3431–3436 (2012).
27. I. Hamada, M. Otani, *Phys. Rev. B* **82**, 153412 (2010).
28. J. Kim et al., *Science* **342**, 833–836 (2013).
29. J. Kang, D. Shin, S. Bae, B. H. Hong, *Nanoscale* **4**, 5527–5537 (2012).
30. R. R. Nair et al., *Science* **320**, 1308 (2008).

# Ultimate Permeation Across Atomically Thin Porous Graphene

Kemal Celebi,[1]* Jakob Buchheim,[1]* Roman M. Wyss,[1] Amirhossein Droudian,[1] Patrick Gasser,[1] Ivan Shorubalko,[2] Jeong-Il Kye,[3] Changho Lee,[3] Hyung Gyu Park[1]†

A two-dimensional (2D) porous layer can make an ideal membrane for separation of chemical mixtures because its infinitesimal thickness promises ultimate permeation. Graphene—with great mechanical strength, chemical stability, and inherent impermeability—offers a unique 2D system with which to realize this membrane and study the mass transport, if perforated precisely. We report highly efficient mass transfer across physically perforated double-layer graphene, having up to a few million pores with narrowly distributed diameters between less than 10 nanometers and 1 micrometer. The measured transport rates are in agreement with predictions of 2D transport theories. Attributed to its atomic thicknesses, these porous graphene membranes show permeances of gas, liquid, and water vapor far in excess of those shown by finite-thickness membranes, highlighting the ultimate permeation these 2D membranes can provide.

Recent advances in graphene synthesis and processing (*1–3*) have enabled demonstrations of atomically thin two-dimensional (2D) membranes showing mechanical sturdiness and hermetic sealing (*4, 5*). Initial attempts to endow mass permeability to the otherwise impermeable graphene have been based on formation of a single aperture (*6*) and randomly etched or defect-originated pores (*7, 8*). However, the macroscopic quantification of mass transport through such 2D pores is extremely challenging because the task demands a large number of pores with controlled dimensions.

We have developed a facile and reliable method for making 2D membranes (Fig. 1, A to G). This process uses chemical vapor deposition (CVD) optimized to grow graphene with minimal defects and good grain connectivity in order to prevent undesirable crack formation (*9*). A clean transfer process places two layers of graphene consecutively onto a SiN$_x$ frame punctured with 49 pores each of 4 μm in diameter (Fig. 1D), forming freestanding graphene layers that are thinner than 1 nm. This double transfer strengthens the freestanding graphene and keeps it from leakage through random defects (*10, 11*). Cleanliness and quality of graphene are found to be crucial during this graphene transfer process because grain boundary defects, polymer residues, or dust particles can induce crack formation while perforating the graphene. Scanning electron microscope (SEM) images (Fig. 1E and fig. S1) support that our transfer process produces crack-free graphene over the length scale of the entire frame. The freestanding film of double-layer graphene remains impermeable to gases and water. Nanopores were then drilled with a focused

ion beam (FIB) to produce porous membranes (Fig. 1, F and G). We used Ga-based FIB to perforate apertures between 14 nm and 1 μm in diameter and He-based FIB for <10-nm-pore drilling. Low exposure doses ($5 \times 10^{-6}$ to $5 \times 10^{-5}$ pA/nm$^2$ for Ga$^+$ ions and $6 \times 10^{-3}$ pA/nm$^2$ for He$^+$ ions) enabled fast and precise drilling, resulting in well-defined pore diameter distributions (Fig. 1, H to K).

The large number of pores ($\sim 10^3$ to $10^6$ per membrane) allows gas flows detectable with conventional mass flow meters. The membranes are mechanically sturdy enough to stand pressure differences of up to 2 bar (higher pressure not tested). N$_2$ flow shows linear pressure dependence (figs. S2 and S3), resulting in pressure-independent permeance. N$_2$ flux displays diameter dependence characterized by two asymptotic theories: free molecular transport (effusion) and modified Sampson's model (*12, 13*) for small- and large-size apertures, respectively (Fig. 2A). For apertures smaller than 50 nm, the mean free path (λ) becomes larger than the aperture diameter (*d*), and the probability of having intermolecular collisions in the vicinity of the aperture decreases. Here, the transport enters the molecular flow regime featured by effusion for small apertures. Knudsen numbers (λ/*d*) for membranes (7.6 nm < *d* < 50 nm) are between 1 and 10, which is well within the molecular flow regime, and so the flow can be explained by the effusion mechanism, which is purely dependent on the probability of a molecule hitting the aperture. This can be quantified by the effusion flux, $Q_E = \bar{u}\Delta n/4 = \Delta P/\sqrt{2\pi m k_B T}$, where *n* is the gas number density, $\bar{u}$ is the mean molecular speed, *P* is the pressure, $k_B$ is the Boltzmann constant, *T* is the temperature, and *m* is the molecular weight. As the pore diameter enlarges, more molecules interact with one another near the aperture, causing a transition from effusion to a more collective flow. However, collective flow models based on pore wall interactions (the Hagen-Poiseuille model) are not suitable to explain the flow behavior for atomically thin membranes. Such flows through an

[1]Nanoscience for Energy Technology and Sustainability, Department of Mechanical and Process Engineering, Eidgenössische Technische Hochschule (ETH) Zurich, Sonneggstrasse 3, CH-8092 Zürich, Switzerland. [2]Laboratory for Electronics/Metrology/Reliability, EMPA (Swiss Federal Laboratories for Materials Science and Technology), Überlandstrasse 129, CH-8600 Dübendorf, Switzerland. [3]Materials and Components R&D Laboratory, LG Electronics Advanced Research Institute, 38 Baumoe-ro, Seocho-gu, Seoul 137-724, Korea.

*These authors contributed equally to this work.
†To whom correspondence should be addressed: parkh@ethz.ch

Downloaded from www.sciencemag.org on February 5, 2015